

Article

# Caribbean Air Chemistry and Dispersion Conditions

Mark R. Jury <sup>1,2</sup> 

<sup>1</sup> Physics Department, University of Puerto Rico, Mayagüez, PR 00681, USA; mark.jury@upr.edu

<sup>2</sup> Geography Department, University of Zululand, KwaDlangezwa 3886, South Africa

Received: 1 May 2017; Accepted: 14 August 2017; Published: 16 August 2017

**Abstract:** The meteorological influences on Caribbean air chemistry are studied using in-situ, satellite and model data. Although African dust plumes join locally generated pollutants, concentrations are relatively low in the eastern Caribbean due to geographic remoteness and steady oceanic trade winds. Urban-industrial emissions from big cities (e.g., Kingston, Santo Domingo, San Juan), agricultural emissions from the south, and volcanic emissions from Montserrat contribute a noticeable burden. Conditions over Puerto Rico in the dry season (December–May) provide a focus for statistical analysis of air chemistry constituents and weather variables that describe dispersion conditions. Monthly and daily air indices are formed by summing the normalized values of fine aerosols and particulates, long- and short-lived trace gases from in-situ, satellite and model sources. The spatial correlation of a daily Puerto Rico air index onto regional dewpoint temperature, air pressure and outgoing longwave radiation fields in December–May 2005–2015 reveals the northward movement of a dry tongue and trough. At the climate timescale, Pacific El Nino conditions favor an increase of spring-time air pollution corresponding to anomalous inflow from Africa and the southern Caribbean coast. Composite weather patterns for a group of high air index values reflect divergent trade winds and a strong jet stream that imparts anticyclonic vorticity, subsidence and low humidity. This new understanding will underpin better air quality forecasts for Puerto Rico and the wider Caribbean.

**Keywords:** Caribbean; air chemistry; Puerto Rico index; weather patterns

---

## 1. Introduction

### 1.1. Background

The Caribbean region and its Antilles islands, lying between North and South America, experience a sub-tropical climate. Trade winds and dry weather that prevail much of the time are interspersed with passing troughs and cyclones in summer. Air pollution concentrations tend to be low, yet levels are rising due to rapid growth in transport, industrial and energy-related emissions [1]. Air quality does not always meet international guidelines [2] due to local and remote emissions, and short-periods of quiescent weather [3–7]. Most of the population live in urban areas, resulting in air pollution hot spots [8–11] in cities such as Caracas, Kingston, Ponce and Santo Domingo. Air pollutants often accumulate during the dry season in wind shadows to the west of mountains. Air quality monitoring and field surveys across Latin America [10,12–16] have improved our understanding, but logistical and technical issues contribute to data gaps.

Satellites have provided observations of atmospheric constituents since 1980 [17]. In 2004, NASA launched the Atmospheric Infrared Sounder (AIRS) and Ozone Monitoring Instrument (OMI) for trace gas retrievals [18]. The MODIS satellite near-infrared radiometer and AURA satellite Cloud-Aerosol Lidar and Infrared Pathfinder Satellite Observation (CALIPSO) [19] retrieve aerosols >0.1  $\mu\text{m}$  diameter with good accuracy. Yet remote sensing of air chemistry suffers from multi-day revisit cycles that may be contaminated by clouds. Locally generated emission plumes have narrow dimensions that depend on wind trajectory and planetary boundary layer (PBL) height; so ground-based measurements tend

to fluctuate. Coupled meteorological models with air chemistry data assimilation such as Modern Era Reanalysis for Research and Applications version 2 (MERRA2) [20,21] help resolve the shortcomings, and provide globally complete records that benefit from detailed emission inventories.

The local concentration of trace gases and aerosol particles is governed by atmospheric dispersion conditions that drive transport, mixing and transformation. Statistical modeling of historical observations can reveal the sensitivity of air pollutants to interdependent meteorological parameters [22,23]. Air chemistry studies around the Caribbean have tended to focus on summer-time African dust plumes and their impact on visibility and human health [7,24–30]. The African dust suppresses easterly waves [31–37] and nitrifies soils across the region [33,38–41].

Agricultural emissions and consequent smoke plumes from Africa and the Amazon reach the Caribbean in spring [4,42]. They contain black carbon (BC) which alters the albedo and rainfall patterns [4,43]. Biomass burning also occurs on the southern coast (Venezuela) and within the Antilles Islands [44]. Overall, the Caribbean accounts for ~1% of global greenhouse gas emissions (Table 1a), totaling 193.5 M T/year (CO<sub>2</sub> equivalent). Energy, industrial and transport emissions from urban areas contribute three-quarters of total (Table 1b), in contrast with agricultural, waste and land-use emissions from rural areas.

**Table 1.** (a) Greenhouse gas emissions (ranked) and population, and (b) contribution per sector in the Caribbean.

Country	(a)		(b)	
	Greenhouse Gas Emissions M T/year	Population M	Sector	Percent
Trinidad and Tob	57.8	1.36	Energy	52.8
Cuba	55.1	11.39	Agriculture	12.4
Dominican Rep	33.8	10.53	Industry	11.2
Jamaica	12.1	2.79	Transport	9.7
Haiti	8.7	10.71	Urban	6.3
Neth. Antilles	5.3	0.20	Waste	5.8
<b>Puerto Rico</b>	<b>5.1</b>	<b>3.68</b>	Land use	1.1
Bahamas	4.7	0.39	Other	0.7
Guadeloupe	2.6	0.47		
Martinique	2.5	0.40		
Barbados	1.4	0.28		
Grenada	0.7	0.11		
Montserrat	0.6	0.01		
Saint Lucia	0.6	0.18		
Antigua and B	0.5	0.09		
Cayman I	0.4	0.06		
Aruba	0.4	0.10		
Dominica	0.3	0.07		
St Vincent and G	0.3	0.11		
St Kitts and N	0.2	0.06		
Anguilla	0.1	0.03		

## 1.2. Motivation and Objectives

Antilles islands such as Puerto Rico have economies dominated by service delivery and manufacturing, with high rates of energy and resource consumption. Despite orderly waste management and a stable, aged population, hospitalization for respiratory complaints is moderate (~0.106) [45]. Air pollution in other Antilles islands is higher: Santo Domingo is #56 and Kingston is #71 out of 330 world cities >1 M pop. [46,47]. There are two types of pollutants: (i) locally generated urban-industrial emissions of short-lived trace gases and particulates; and (ii) remotely sourced (Saharan) fine dust aerosols and agricultural emissions from (Amazon) biomass burning that include BC, carbon monoxide (CO) and ozone (O<sub>3</sub>). Air chemistry affects the earth's heat budget and ecological services, hence we are motivated to understand and mitigate the problem.

The main objective of this study is to characterize the Caribbean air chemistry and atmospheric dispersion at daily to multi-year timescales, using in-situ, satellite and model products. It is proposed that Puerto Rico represents a typical Antilles island pollution hotspot; temporal analyses derive therefrom. The scientific questions include: (i) what is the spatio-temporal distribution of air constituents? (ii) do air pollution episodes relate to certain climate and weather patterns? (iii) what statistical relationships can be used to underpin air quality forecasts?

## 2. Data and Methods

### 2.1. Data

The Caribbean study area (Figure 1a) 10–24° N, 79–54° W extends from Trinidad to Cuba. Current information on country emissions and sector burdens were drawn from the Food and Agriculture Organization [48] database, and fire emission data were obtained from the Global Fire Emissions Database (GFED) [49]. In-situ [50] sun photometer data at Parguera, Puerto Rico, was considered and the daily aerosol optical depth fine fraction (AOD f/c) was extracted. After screening for deep clouds, the 2005–2015 sample size was 2880 days. Monthly Puerto Rico hospital respiratory case admissions were obtained from the Dept of Health [45]. The information is “diagnosed in-patient totals”, but some values appear rounded or constant. Hence, only the annual cycle was used.

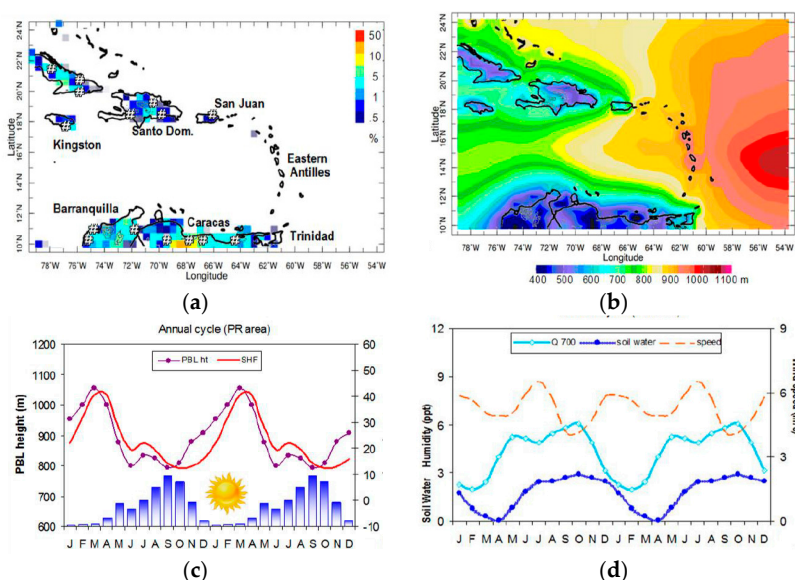


**Figure 1.** (a) Caribbean region Global Fire Emissions Database (GFED) fire density (shaded) and cities >500 K hash-mark; (b) 2005–2015 average MERRA2 planetary boundary layer (PBL) height (m). Mean annual cycle  $\times 2$  of (c) PBL, sensible heat flux (SHF), rain (bars up to 5 mm/day); (d) 700 hPa specific humidity, soil water (cm) and surface wind speed. Sun icon in (c) represents dry season.

The MERRA2 GEOS5 reanalyses [20] provided fields of monthly aerosol and trace gas. Here the aerosol optical thickness (AOT) fraction for particulates  $<2.5 \mu\text{m}$  in the 1000–925 hPa “near-surface” layer is utilized. Satellite aerosol observations from OMI-Aura include: aerosol optical thickness (AOT) fraction by absorption at  $0.483 \mu\text{m}$ , and aerosol index (AI) by UV backscatter [51–54].

MERRA2 air chemistry data yielded monthly fields of near-surface BC ( $<10 \mu\text{m}$ ), CO, O<sub>3</sub>, and sulphur dioxide (SO<sub>2</sub>) concentration, at  $\sim 50 \text{ km}$  resolution from January 1980–December 2015. The MERRA2 monthly and daily weather variables that describe atmospheric dispersion include: surface (2 m) air and dewpoint temperature (Tdew), sea level (SL) air pressure, surface-layer (10 m) wind speed and wind direction, 600 hPa vertical motion, turbulence-inferred PBL height, and sensible heat flux (SHF). Derived meteorological variables include lapse rate  $dT/dz$ : 850 hPa minus 1000 hPa air temperature, relative

divergence:  $dU/dx + dV/dy$ , and relative vorticity:  $dV/dx - dU/dy$ . The MERRA2 assimilation system receives steady inputs from surface measurements, weather observations and emission inventories, but incremental inputs from satellites that measure fine aerosols (1980+) and tropospheric trace gases (2000+).

Daily trace gas air chemistry fields from January 2005–December 2015 were obtained in the 1000–925 hPa layer for CO and O<sub>3</sub> from the AIRS satellite [55] at 100 km resolution. Cloud-screened tropospheric NO<sub>2</sub> [56] and PBL SO<sub>2</sub> [57] were obtained from OMI-Aura at 25 km resolution. Daily NOAA satellite outgoing longwave radiation (OLR) [58] was used to infer cloud presence and depth, CMORPH rainfall was obtained [59] and CALIPSO aerosol profiles over Puerto Rico were averaged to study vertical distribution [60]. Table 2 summarizes the datasets, acronyms and characteristics.

**Table 2.** Datasets used in the analysis.

Acronym	Name	Space, Time Resolution	Quantity
AERONET	Sun photometer 0.55 $\mu\text{m}$ (Parguera)	Station, daily	AOD fine fraction
AIRS	Atmospheric Infrared Sounder	100 km, twice daily	CO, O <sub>3</sub> 1000–925 hPa
CALIPSO	Cloud-Aerosol Lidar and Infrared Pathfinder Satellite Observation	~1 km along swath, weekly	Aerosol density profile
CMORPH	CPC morphed multi-satellite fields	25 km, 3 hourly	Rainfall
GEOS-5	Air chemistry data assimilation system input to MERRA2	~50 km, daily, monthly	Smart interpolation scheme
GFS	Global Forecast System, operational weather data	50 km, 3 hourly	Forcing of HYSPLIT model
GRACE	Gravity Recovery and Climate Experiment	100 km	Soil water fraction
HYSPLIT	Hybrid Single Particle Lagrangian Integrated Trajectory Model	~25 km, along trajectory	Backward trajectories
MERRA2	Modern Era Reanalysis for Research and Applications	~50 km, daily, monthly	BC, O <sub>3</sub> , SO <sub>2</sub> , AOT, meteorology
MODIS	Moderate Imaging Spectrometer (Near-infrared sensor, $\lambda$ 0.5–2.0 $\mu\text{m}$ )	100 km, twice-daily composite	Aerosol optical depth
NAM	North American Mesoscale weather model (WRF)	10 km, 3 hourly	Local Meteorological fields
NCEP2	National Centers for Environmental Prediction version2 reanalysis	200 km, monthly	Regional Meteorological fields
NWS	National Weather Service (San Juan)	Radiosonde–twice-daily	Temp and wind profiles
OLR	Outgoing Longwave Radiation	100 km, daily	Surface or cloud top infrared emission
OMI	Ozone Monitoring Instrument UV absorption $\lambda$ 0.31–0.46 $\mu\text{m}$	25 km, daily	tropospheric NO <sub>2</sub> , PBL SO <sub>2</sub> , AOT

## 2.2. Temporal Analysis

Time series (monthly 1980–2015, daily 2005–2015) were formed by averaging model and satellite data over Puerto Rico: 17.75–18.75° N, 67.5–65.5° W. Daily satellite retrievals required the additional step of calculating a 3-day running maximum to alleviate missing swaths. Individual air chemistry time series were pair-wise correlated, and normalized and summed to produce aggregate indices. The monthly Puerto Rico air index is MERRA2 model-based and is derived from the sum of standardized values of near-surface aerosol PM<sub>2.5</sub>, BC PM<sub>10</sub>, CO, O<sub>3</sub> and SO<sub>2</sub>. The daily Puerto Rico air index is derived from the sum of standardized values of in-situ AOD f/c and satellite-based near-surface CO, O<sub>3</sub>, AOT and NO<sub>2</sub>. The mean annual cycle of the air chemistry indices and Puerto Rico hospital respiratory case admissions was calculated in the period 2005–2015, to identify the dry season of higher impact: December to May. The air indices were subjected to wavelet spectral analysis to evaluate the significant pulse frequencies.

Statistical analyses were performed via Pearson product-moment cross-correlation of air constituents and weather variables. Although record length is 4018 days (2005–2015), statistical significance at 90% confidence was evaluated according to the degrees of freedom as deflated by persistence and filtering,

hence  $r > |0.25|$  for continuous data with annual cycle retained. In addition to pair-wise associations, 12 candidate meteorological predictors were regressed onto the daily air index. Eliminating predictors below 90% confidence, a final algorithm emerged.

### 2.3. Spatial Analysis

To understand inter-annual climate influences, the December–May 1980–2015 monthly Puerto Rico air index was correlated with fields of MERRA2 surface air pressure and temperature, GRACE satellite soil moisture [61] and NCEP2 reanalysis winds [62] over the area: 20° S–35° N, 160° W–20° E. The maps reveal the field co-variance with Puerto Rico air quality. The sample size is 36 years; June–November months are removed, and  $r > |0.40|$  achieves 90% confidence.

The study of regional weather controls in the period December–May 2005–2015, the daily Puerto Rico air index  $>0.8$  (upper half) was correlated with MERRA2 fields of surface Tdew, SL air pressure and NOAA satellite OLR in the area: 0–35° N, 95–35° W, 5 days before and concurrent. The sample size is 1430 days, so  $r > |0.15|$  is significant at 90% confidence with  $>100$  degrees of freedom.

Air pollution events were studied for days with Puerto Rico air index  $>1.1$  (upper 10%) and OLR  $>260$  W/m<sup>2</sup>. The consequent 18 days were composite averaged and MERRA2/NCEP2 fields of surface and upper wind, humidity, meridional and zonal circulation were analyzed for structure. The highest ranked events of 4 March 2012 and 29 April 2014 were studied for atmospheric transport and dispersion. A CALIPSO aerosol backscatter slice [63] and San Juan NWS radiosonde profile were obtained, and back-trajectories were calculated using the HYSPLIT model [64] initialized with GFS weather data. To focus on island-scale dispersion conditions, Puerto Rico maps of NAM wind and temperature fields, and in-situ weather station data from Mayaguez are studied.

Scientific inferences depend on statistical inter-comparison, spatial correlation, composite pattern and case study features that reveal atmospheric dispersion, using a Puerto Rico air index as temporal “pointer”, using methods similar to [65]. All model products used here are “hindcast” and consequently represent a sophisticated interpolation of in-situ and satellite air chemistry and meteorological data.

## 3. Results

### 3.1. Mean Climate

The PBL, which contains the air pollutants affecting health, thins from east to west across the Caribbean (Figure 1b). The mechanical and thermal influences of friction, nocturnal cooling and upwelling tend to limit PBL height in the wind shadow zones of the larger Antilles Islands and along the southern coast. A thicker PBL characterizes the tropical Atlantic where trade winds are strong.

The mean annual cycle of local weather variables (Figure 1c,d) reflects steady trade winds but amplified hygro-thermal changes. In the December–April dry season, rainfall is negligible and the PBL and SHF grow in March–April as soil moisture and vegetation fraction diminish.

### 3.2. Mean Air Chemistry

The Caribbean-wide distribution of trace gases and particulates displays hot spots (Figure 2). MERRA2 model mean CO concentrations (and BC) are low in the tropical Atlantic and higher over Jamaica, Cuba, Hispaniola and Venezuela (Figure 2a). The OMI UV aerosol index (Figure 2b) reflects the Saharan dust plume east of the Antilles, while AOD PM<sub>2.5</sub> shows a plume over the southeastern Caribbean due to agricultural smoke plumes from central Africa and the Amazon. NO<sub>2</sub> reflects near-surface urban-industrial emissions (Figure 2c). Puerto Rico values are lower than Jamaica, Cuba, Hispaniola, and Venezuela, likely due to the capital city being windward. Similarly, near-surface SO<sub>2</sub> concentrations are low east of the Antilles (Figure 2d), but higher over the big cities of Kingston, Santo Domingo, Caracas, and the Montserrat volcano.

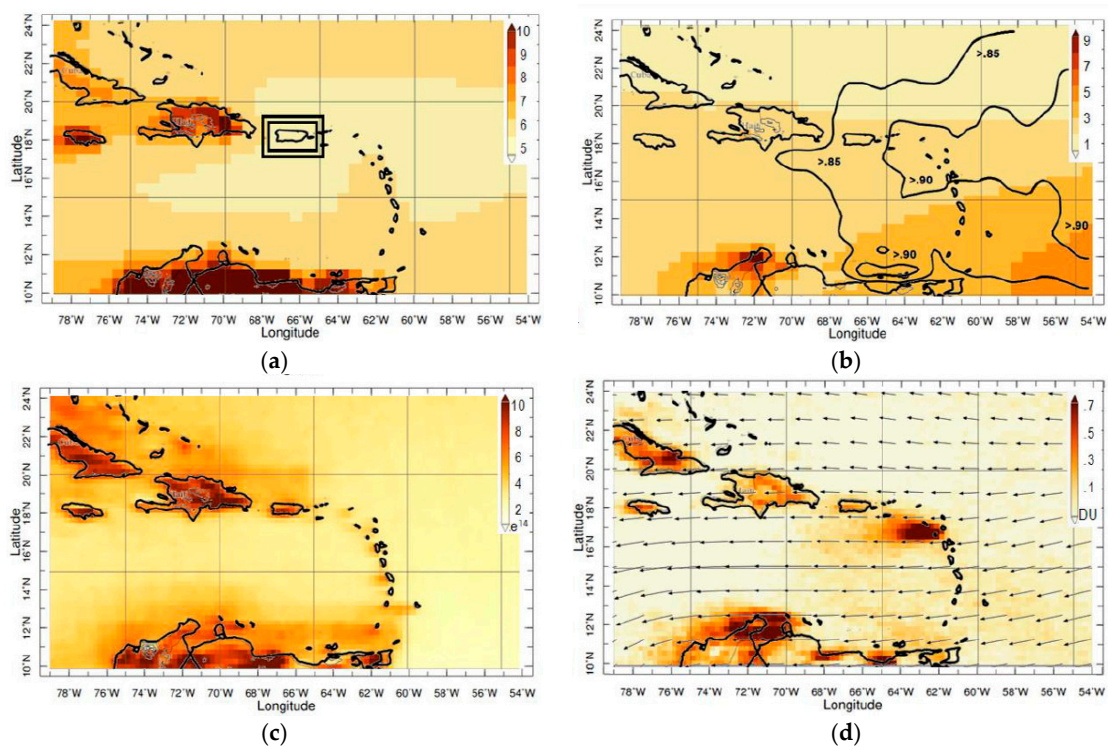


**Figure 2.** Mean (2005–2015) maps of near-surface: (a) MERRA2 CO in  $10^{-6}$  g/kg with index area (box); (b) MERRA2 aerosol PM<sub>2.5</sub> shaded ( $10^{-6}$  g/m<sup>3</sup>) and OMI UV aerosol index (contour > 0.85); (c) OMI NO<sub>2</sub>  $10^{15}$  molecules/cm<sup>2</sup>; (d) OMI SO<sub>2</sub> in DU with wind vectors.

The mean annual cycle of agricultural emissions BC and CO peak in January–April (Figure 3a), whereas the aerosols, O<sub>3</sub> and SO<sub>2</sub> rise in June–October. Summed together, the overlap February–April season shows highest values. The mean annual cycle of the summed air constituents (2005–2015) and Puerto Rico hospital respiratory cases compare in Figure 3b. The satellite air index peaks in March–May and dips in July–August, while model values follow a similar cycle although slightly higher in June/October. Respiratory cases closely follow the air indices except for a dip in September. The variable that relates closest with the mean annual cycle of respiratory cases is Puerto Rico soil moisture ( $r = -0.90$ ). It lags local rainfall and SST by one month, and correlates sympathetically with soil moisture in West Africa. Agricultural burning precedes the seasonal increase in soil moisture.

The 2005–2015 mean vertical and longitudinal distribution of air constituents is illustrated in Figure 3c,d. The CALIPSO aerosol density profile reaches a maximum in the first kilometer above Puerto Rico. The local OMI AOT map (inset) shows higher values downstream from San Juan. The aerosol profile spikes at 700 m and 400 m, well below the trade wind inversion. The longitudinal distribution of aerosols and trace gases averaged in Puerto Rico latitudes is quite instructive. Saharan dust diminishes westward in a second-order trend, undulating downward at 55 °W and upward at 63 °W. Standard deviations are high, due to variability in the arrival of African dust plumes. The longitudinal mean NO<sub>2</sub> is low in the east, and rises westward over the urban centers, peaking near San Juan (66 °W) and Kingston (78 °W). Near-surface O<sub>3</sub> is also low in the open Atlantic and rises to a peak over Santo Domingo (72 °W). Ostro et al. [66] found that ambient NO<sub>2</sub> dose significantly affects respiratory health.

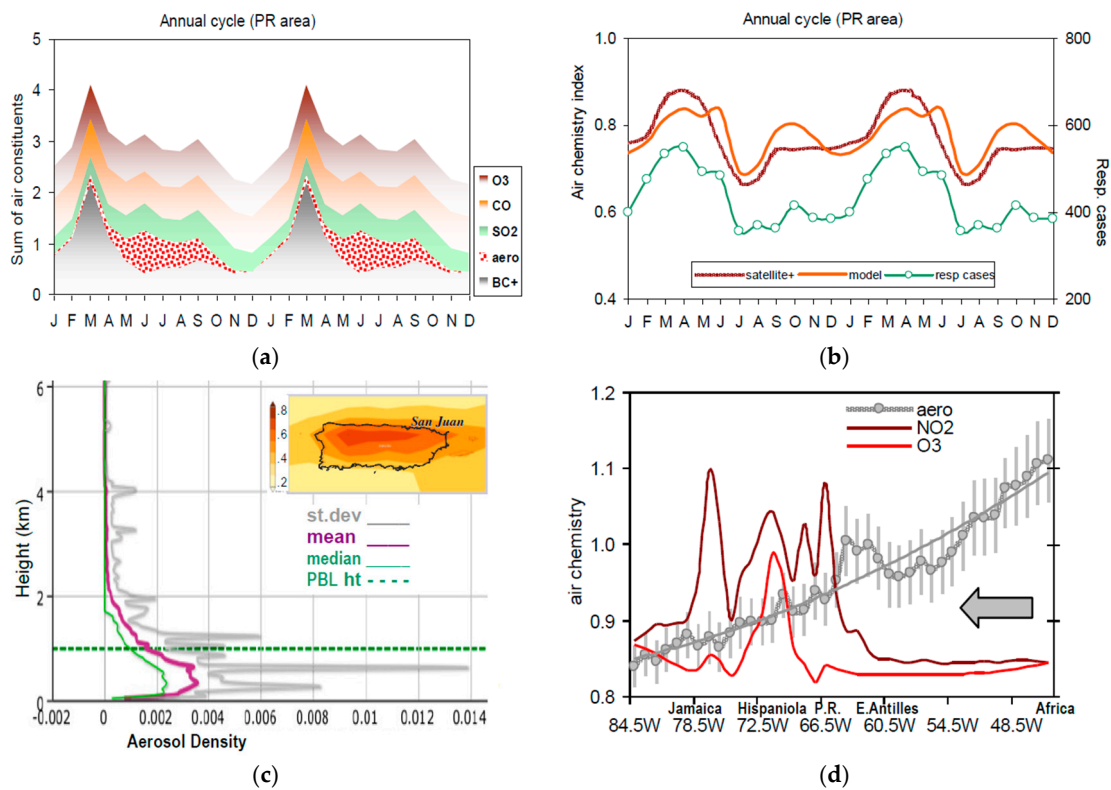


**Figure 3.** (a) Sum of normalized air constituents; (b) Mean annual cycle  $\times 2$  of satellite and model-based air indices and Puerto Rico respiratory cases (2005–2015); (c) CALIPSO mean aerosol profile over Puerto Rico and OMI AOT map inset; (d) Longitude (W–E) analysis of mean air constituents average 17.5–19° N with aerosol trend and standard deviation (bars) and arrow for wind flow.

### 3.3. Monthly Statistics and Correlation Maps

Monthly time series of MERRA2 PBL height and air chemistry over Puerto Rico since 1980 (Figure 4a,b) reveal a corresponding annual cycle and year-to-year fluctuations. After 2000, the air index becomes more chaotic, presumably due to the inclusion of satellite data. Its wavelet spectra show that one-year cycles are replaced by half-year cycles around 2000 (Figure 4b). After filtering, the Puerto Rico air index displays significant 7-year cycles and a 3-year rhythm after 2005 (Figure 4c). The SL air pressure and SST correlation maps with respect to the December–May air index (Figure 4d,e) point to Pacific El Niño as an influence, similar to [67]. Above normal SST in the equatorial zone and a (low) trough extending into the Northeast Pacific correspond with higher air pollutants. Below normal SST in the South Atlantic and a (high) ridge extending into the African Sahel form part of this pattern of influence at the climate time scale. The soil moisture correlation map (Figure 4f) reveals dry conditions over the northern Amazon Basin and West Africa, suggesting a higher probability of biomass burning and fire emissions. The wind correlation map reflects Pacific El Niño (westerly) circulation anomalies and a local conveyor belt. Easterly wind anomalies in the equatorial Atlantic sweep over the northern Amazon and into the Caribbean.

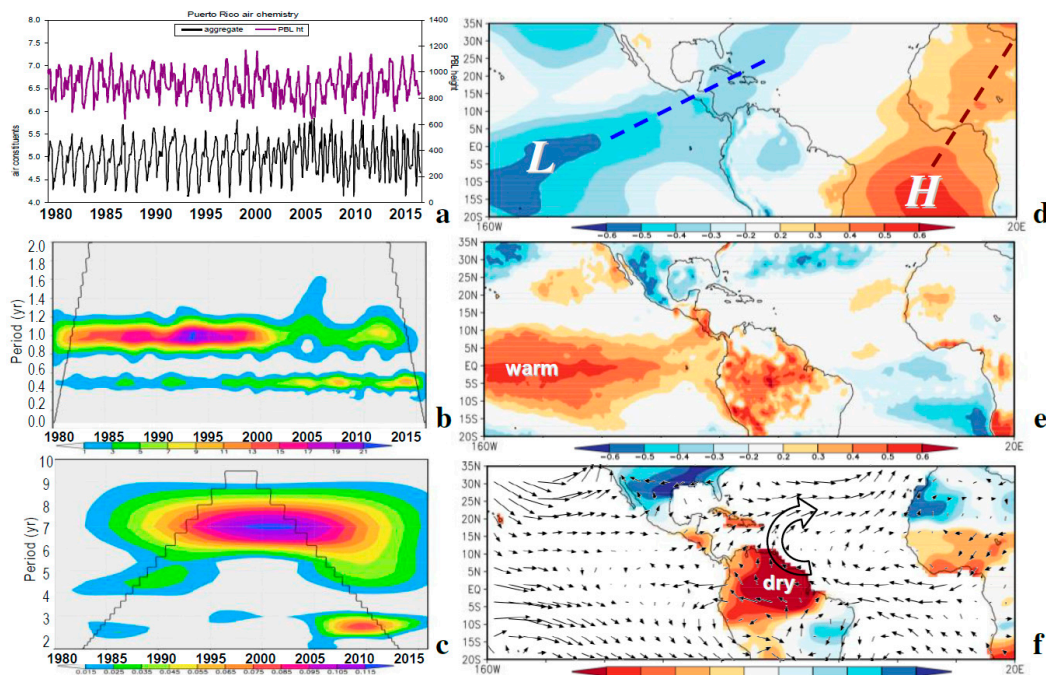


**Figure 4.** (a) Monthly time series of model-derived Puerto Rico air index and PBL height. Air index wavelet spectra (b) unfiltered and (c) 18-month smoothed, with cone of validity. Correlation maps of December–May air index with respect to: (d) MERRA2 air pressure; (e) surface temperature; (f) GRACE soil moisture and 1000–850 hPa layer wind (correlation vectors, max = 1).

The monthly Puerto Rico air index (cf. Figure 4a) correlates +0.42 with the zonal winds, meaning that lighter trades accumulate pollutants at seasonal time scale. The monthly statistics cover a minor aim; the major objective is short-term fluctuations of air quality and dispersion.

### 3.4. Daily Statistics and Correlation Maps

Table 3 lists the daily correlations and reveals significant values for AOD f/c with respect to OLR, Tdew, U wind and SHF. O<sub>3</sub> and CO display similar relationships to weather variables: negative with Tdew and positive with SHF (cf. scatterplots Figure 5a). AOT is weakly negative correlated with OLR, while NO<sub>2</sub> shows little sensitivity or agreement with weather variables and air constituents, perhaps being more local/episodic than remote/seasonal. Naturally, the air index (Figure 5a) is related with its constituents: CO  $r = +0.61$ , O<sub>3</sub> + 0.60, NO<sub>2</sub> + 0.56, AOD f/c + 0.44, AOT + 0.39; and also with certain meteorological variables: SHF +0.46 and Tdew −0.37, indicating that warm dry weather helps liberate, suspend and accumulate particles and gases over Puerto Rico. Tdew is negatively related with SHF (cf. Figure 5a) and consequently to surface heating over the island. In respect to respiratory complaints, Newhouse and Levetin [68] found correlation with low Tdew/humidity, while Gent et al. [69] noted correlation with high O<sub>3</sub>/air temperature. Here, a multi-variate regression of 12 candidate meteorological predictors, subsequently reduced to +SHF and −Tdew to predict 22% of daily pollution variability.

The daily Puerto Rico air index time series (cf. Figure 5b) displays spiky episodes with a background annual cycle. Maxima appear in March–April while minima spread across the August–October wet season. The air index wavelet spectra (Figure 5c) display short-lived events with a significant 8–16 day rhythm. There is little spectral energy below 7 days, suggesting that easterly waves play little role in pulsing the air quality. Westerly troughs in spring contribute more influence. There are patches of significant spectral energy around 30 days, possibly linked with equatorial Madden-Julian Oscillation wave interaction with South American smoke plumes.

**Table 3.** Pair-wise correlation of daily air index, individual constituents and weather variables averaged over Puerto Rico (2005–2015); bold >90% confidence. Data sources are denoted m = MERRA2, o = OMI, a = AIRS, AOD f/c = in-situ AERONET, OLR = satellite, weather variables from MERRA2 include: Tdew = dewpoint temperature, U V wind = zonal and meridional components, dT/dz = T850–T1000 hPa, humidity = 850 hPa specific humidity, SH flux = sensible heat flux, evap = latent heat flux.

	N~4000	Index	AOD f/c	m O <sub>3</sub>	o NO <sub>2</sub>	o AOT	a CO
AOD f/c		<b>0.44</b>					
m O <sub>3</sub>		<b>0.60</b>	<b>0.27</b>				
o NO <sub>2</sub>		<b>0.56</b>	0.09	0.07			
o AOT		<b>0.39</b>	−0.12	−0.04	−0.02		
a CO		<b>0.61</b>	<b>0.29</b>	<b>0.68</b>	0.13	−0.04	
OLR		0.13	<b>0.28</b>	0.18	0.03	<b>−0.27</b>	0.20
Tdew		<b>−0.37</b>	<b>−0.25</b>	<b>−0.50</b>	−0.07	0.19	<b>−0.63</b>
U wind		0.11	<b>0.33</b>	0.06	0.03	0.02	0.06
V wind		−0.07	−0.09	−0.15	−0.08	0.17	−0.15
dT/dz		−0.19	−0.11	<b>−0.31</b>	−0.03	0.14	−0.20
humidity		−0.11	0.03	−0.21	0.01	0.14	<b>−0.27</b>
SH flux		<b>0.46</b>	<b>0.30</b>	<b>0.53</b>	0.09	−0.05	<b>0.56</b>
evap		−0.17	−0.21	−0.05	−0.06	−0.11	−0.13

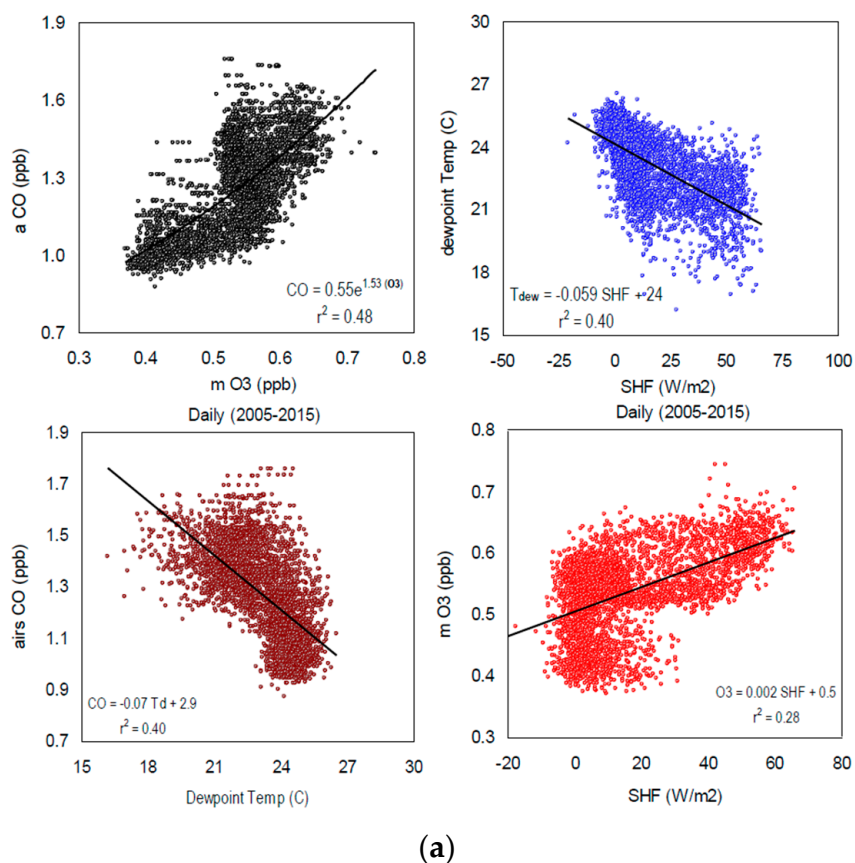
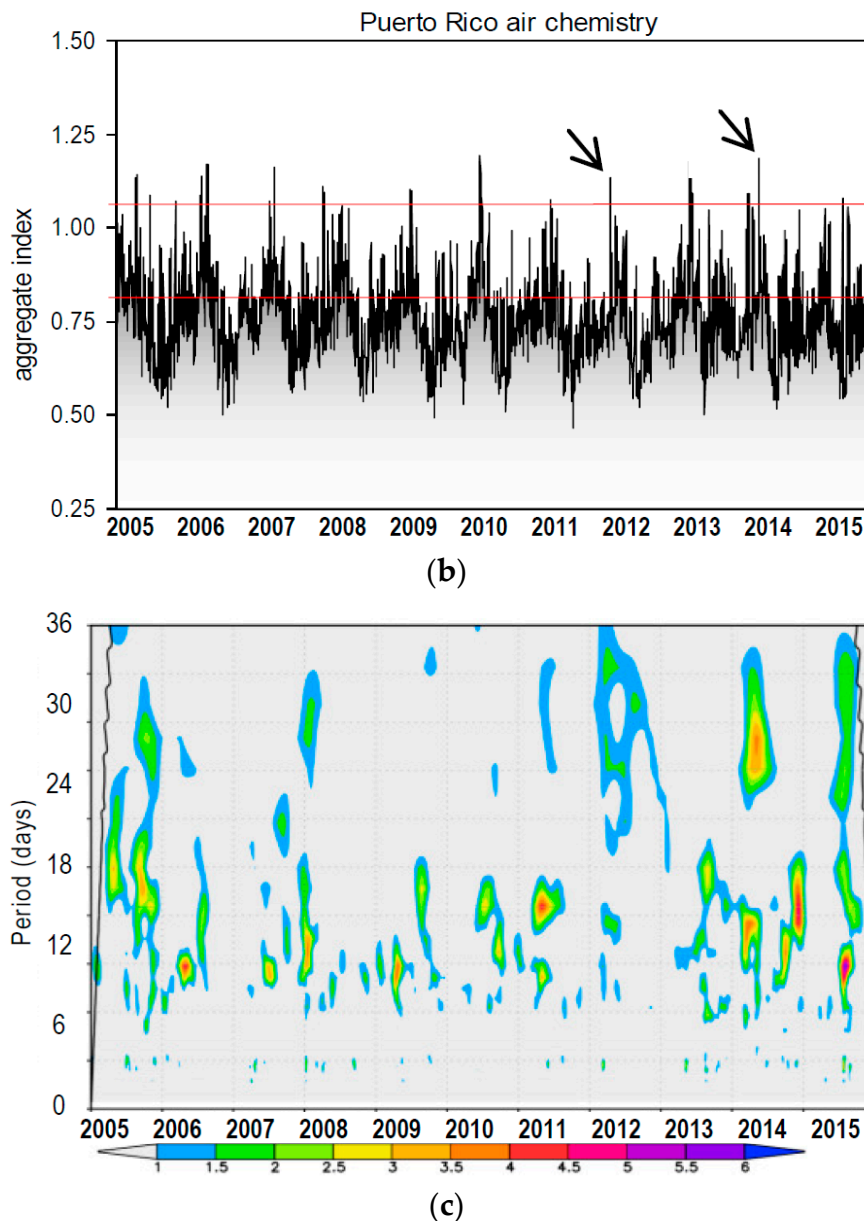


Figure 5. Cont.



**Figure 5.** (a) Scatterplots of daily air constituents and weather variables with regression fit, cf. Table 3; (b) Daily time series of Puerto Rico air index with case studies (arrows) and thresholds (red lines); (c) Wavelet spectral analysis of air index shaded >90% confidence.

Correlation maps are analyzed with respect to the December–May daily Puerto Rico air index  $>0.8$  for Tdew, SL air pressure and satellite OLR in Figure 6a–c. Five days before air pollution rises in Puerto Rico, a dry line ( $-T_{dew}$ ,  $+OLR$ ) extends from Panama to Hispaniola. This feature shifts to the north of Puerto Rico on days with peak concentration. The SL air pressure correlation map five days before, shows a high cell situated over the Gulf of Mexico and a low trough over the Atlantic. The troughs shift northward and a high cell emerges over South America. This pattern limits dispersion, and suggests tropical inflow to a sub-tropical Rossby wave during spring-time pollution episodes.

Northern hemisphere 500 hPa geopotential height correlation maps are illustrated in Figure 6d. Using all index values  $>0.8$ , the pattern consists of a circumpolar ridge in the tropics and a trough north of Puerto Rico. The precursor pattern for values  $>0.8$  in December–May season, displays an elongated upper trough between the Caribbean and Africa that indicates strengthening of the sub-tropical jet (Figure 6d).

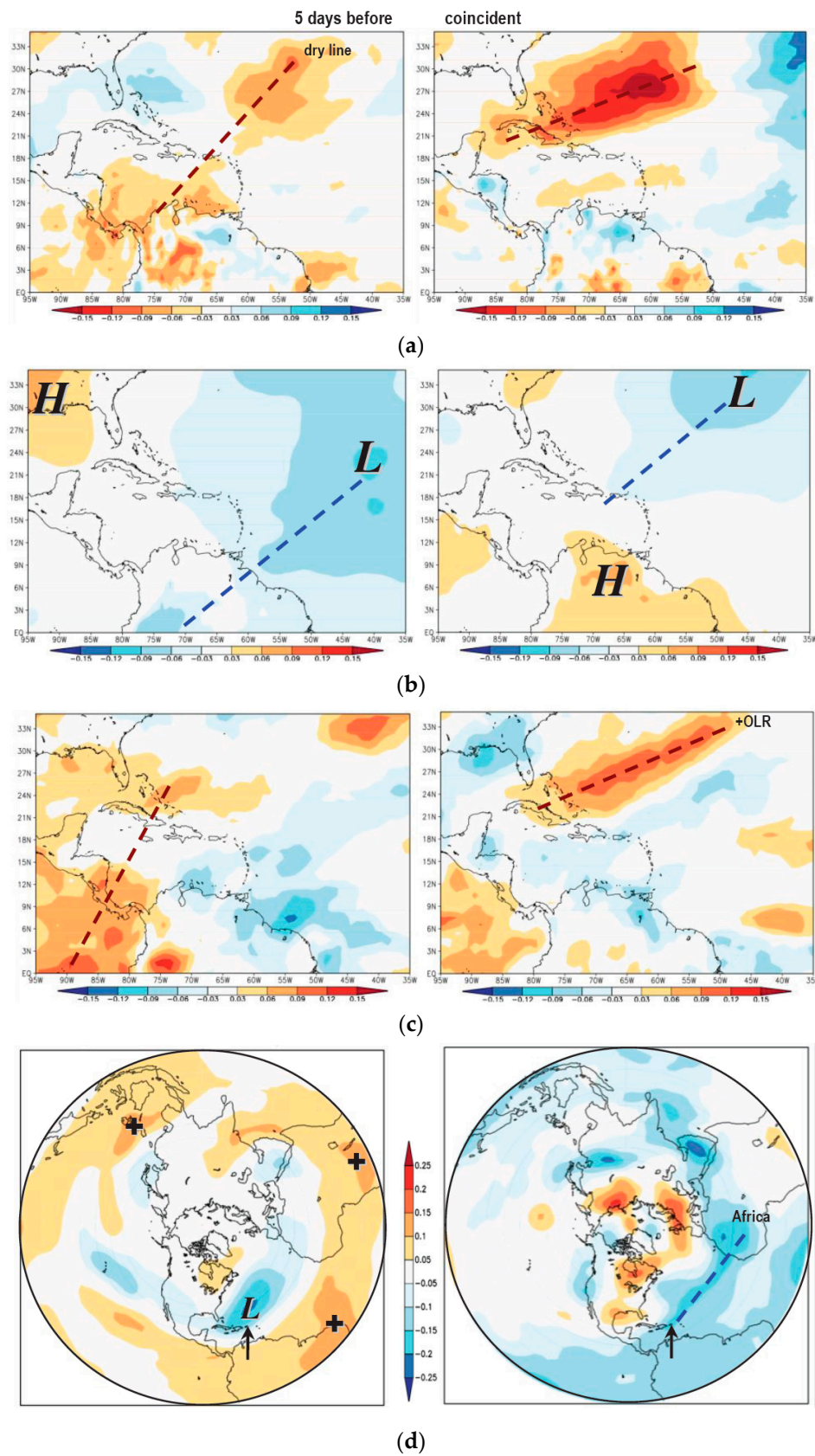


**Figure 6.** Correlation maps of daily December–May Puerto Rico air index >0.8 with respect to: (a) Tdew; (b) SL air pressure and (c) satellite OLR, N = 1430; left = 5 days before, right = coincident; (d) N-polar hemispheric correlation maps of daily Puerto Rico air index and 500 hPa geopotential height, left: all index >0.8, right: December–May index >0.8 at five days before; arrow points to Puerto Rico.

From the daily Puerto Rico air index  $>1.1$ , a group of high cases was selected for analysis (Figure 7). The composite weather appears close to climatology: east-northeast surface trade winds circulate around the North Atlantic High (Figure 7a). There is a NW-axis of anomalous divergence lying upstream from the Caribbean. Upper westerly winds are confluent near Puerto Rico (Figure 7b); indicating a southward shift of the sub-tropical jet from 30 to 18° N. The zonal circulation (Figure 7c) overturns from upper westerly to lower easterly over the central Atlantic. Sinking and drying occur in the 700–400 hPa layer, and the moist marine layer remains thin.

The N–S section shows that air temperatures are warm up to 800 hPa over the Caribbean, and consequently stable (Figure 7d). The Hadley circulation on composite air pollution days (Figure 7e) exhibits a shallow overturning rotor with convergence/rising over South America and divergence/sinking over the Antilles. The zonal circulation (Figure 7f) features an intrusion of anticyclonic vorticity due to the sub-tropical jet stream. The composites suggest accentuated zonal flows that bring dust from Africa and promote anticyclonic divergence and locally warm dry weather. The key feature is a southward shift of the sub-tropical jet stream, causing upper level convergence that limits dispersion.

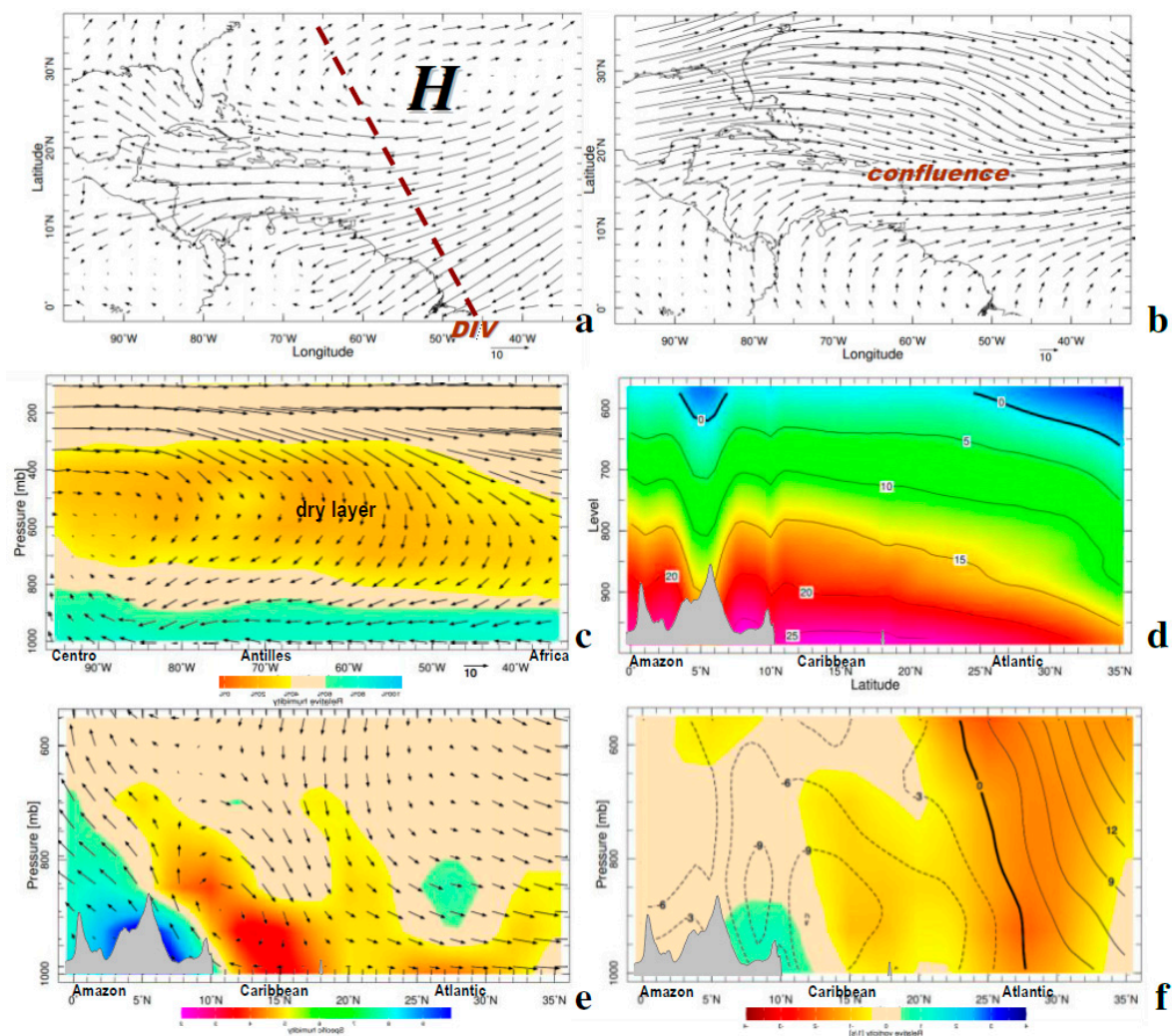


**Figure 7.** Composite weather patterns for the 18 highest cases with Puerto Rico air index  $>1.1$  and  $OLR > 260 \text{ W/m}^2$ : (a) 1000 hPa wind and axis of anomalous divergence (dashed), (b) 200 hPa wind. (c) Composite W–E section of zonal circulation (vectors) and relative humidity (shaded). Composite S–N sections in 65–67.6° W longitude of: (d) air temperature, (e) meridional circulation and divergence (shading  $10^{-5}$ ), (f) zonal wind isotachs and vorticity (shading  $10^{-5}$ ), with topographic profile.

### 3.5. Air Pollution Events

Two prolonged spring season air pollution events are studied. The CALIPSO vertical section on 4 March 2012 (Figure 8a) shows a dense surface layer of aerosols thinning northward. The corresponding San Juan radiosonde profile (Figure 8b) is characterized by a dry inversion layer above 750 hPa. Trade winds give way to upper northerly winds in this case. The 29 April 2014 CALIPSO vertical section (Figure 8c) displays aerosol plumes in a deep layer over the southern Caribbean, while the radiosonde profile shows that winds become westerly above 600 hPa but the dry layer is weak.

HYSPLIT back-trajectories in the two cases (Figure 8e,f) are dominated by westward movement and air parcels ultimately originating from northwest Africa. The trajectories are straighter in the 1–6 March 2012 case, but sweep toward Puerto Rico with anticyclonic curvature in the 25–30 April 2014 case, possibly entraining volcanic emissions from Montserrat. In both cases, the vertical section of back-trajectories indicates steady sinking from the Atlantic to the Antilles. In the 25–30 April 2014 case, the sinking is through a deeper layer, while in the 1–6 March 2012 case the aerosol-laden air reaches the surface well east of Puerto Rico.

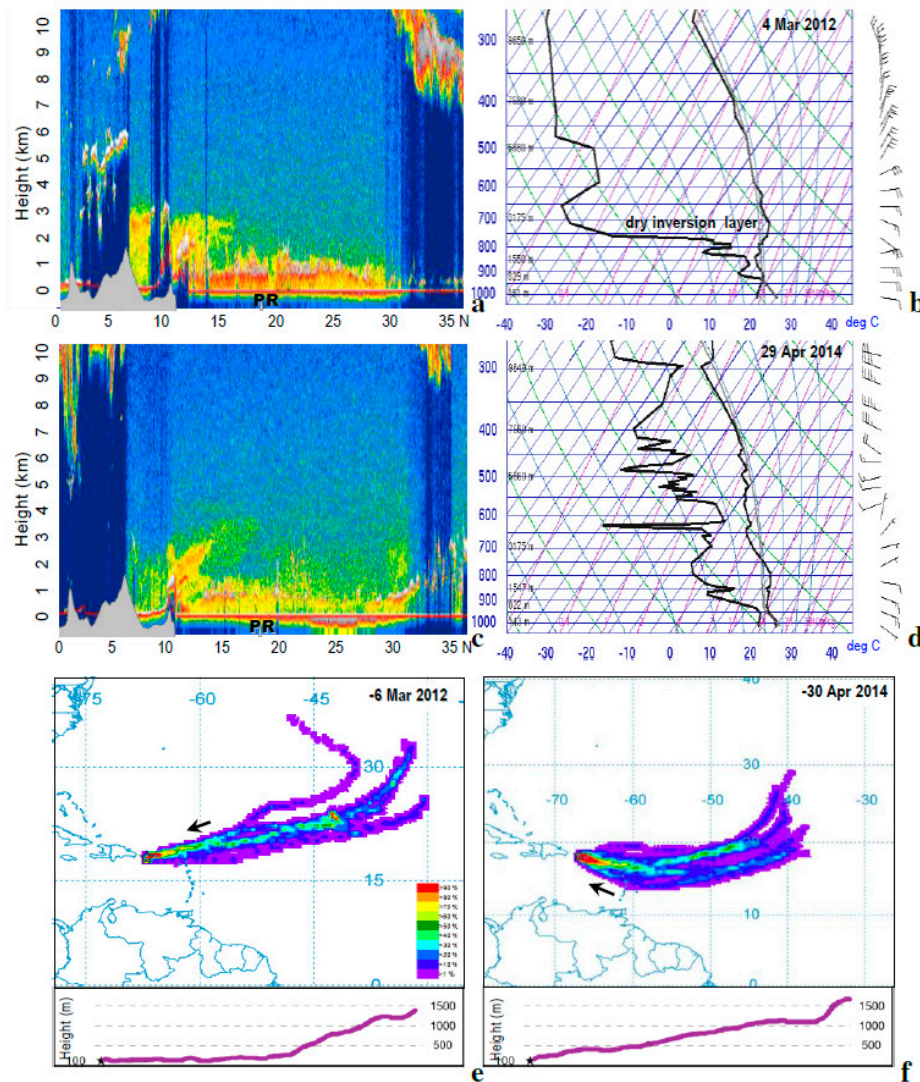


**Figure 8.** CALIPSO S-N section of aerosol density on (a,c) 06UTC 4 March 2012 and 29 April; (b,d) corresponding radiosonde profiles from San Juan. Five-day HYSPLIT back-trajectory probability plots ending on: (e,f) 6 March 2012 and 30 April 2014, with vertical axis in lower panel.

### 3.6. Island Hot Spot

The reader will have noted wind shadows and pollution hot spots in the earlier results (cf. Figures 1b and 2c). These features are analyzed for Puerto Rico using high resolution NAM fields of wind and temperature, and weather station data from the leeward coast (Figure 9a–f). On 4 March 2012 and 29 April 2014, afternoon trade winds >6 m/s converge over the heated island, where SHF exceeds 200 W/m<sup>2</sup>. At Mayaguez on the west coast, a seabreeze >4 m/s blows from 10:00–18:00 due to the horizontal temperature gradient. The seabreeze opposes the trade winds and traps emissions, but may also trigger afternoon showers (i.e., 28 April 2014, Figure 9f).

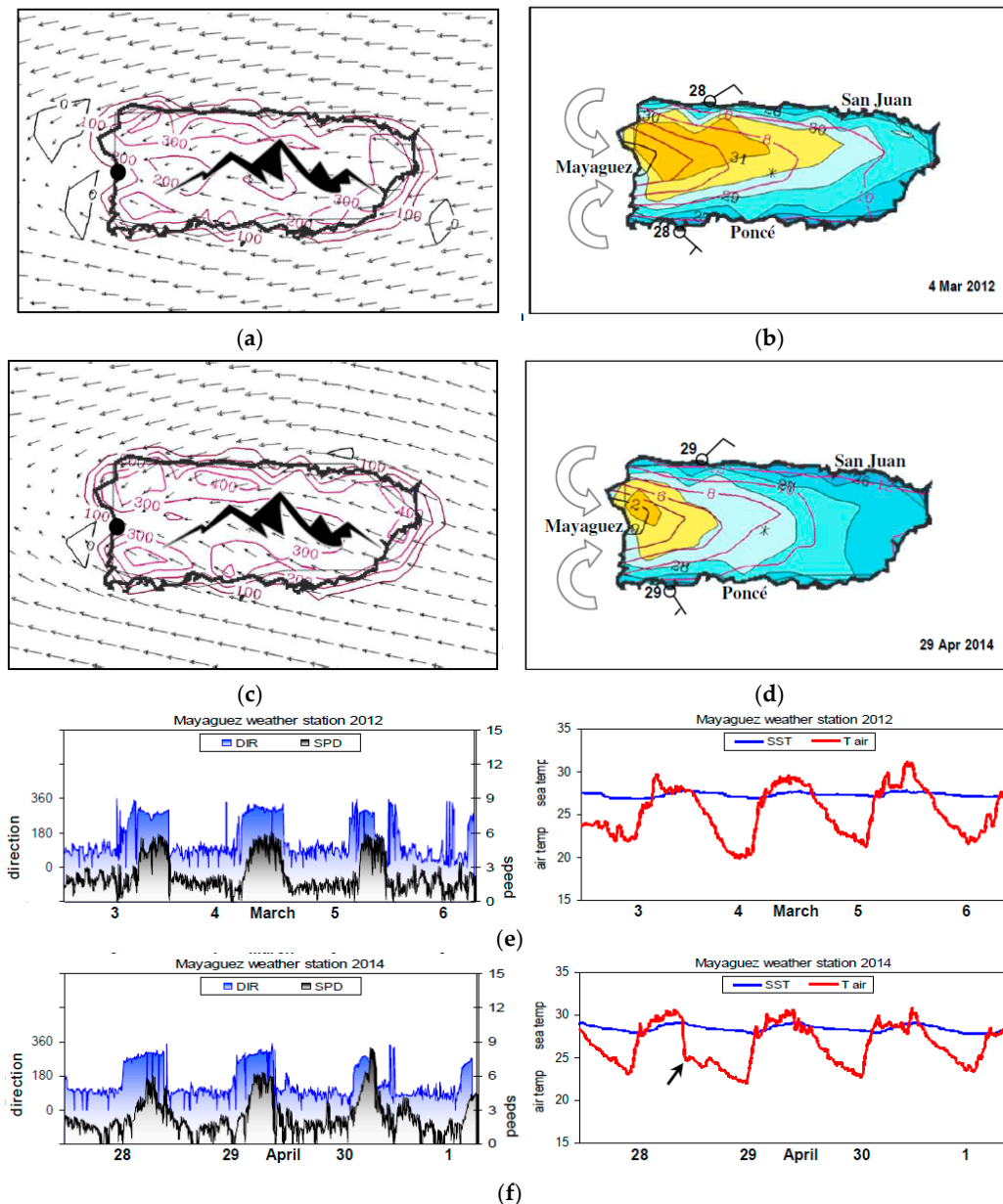


**Figure 9.** Puerto Rico area NAM 14:00 surface fields (a,b) 4 March 2012 and (c,d) 29 April 2014 of wind vectors and SHF with mountain icon (left); wind speed (contour, kt) and air temperature (shaded, °C) with ocean area masked, place names, two station plots, and schematic wind rotors; (e,f) Mayaguez weather station data (dot in (a,c)) during the two events: winds (left, m/s) and temperatures (°C). Arrow in (f) points to rain cooling.

It is during the spring season that SSTs are lowest and help turn the Antilles islands into air pollution sinks. The day-time seabreeze is quantified from [70] as  $\Delta U = ((g H/\theta_0) d\theta/dx) dt$ , where  $dt = 2 \times 10^4$  s,  $g$  is gravity,  $H$  is surface warm layer = 40 m,  $\theta_0$  is potential temperature (300 K) and  $d\theta/dx = 1.5$  K/10<sup>4</sup> m, the inland increase of potential temperature. The inward turning of trade winds also depends on the relationship between PBL airflow, thermal stability and mountain height as described by the Froude number  $F = U/NH$  where  $N = ((g/\theta_0) d\theta/dz)^{1/2}$ , (cf. [71,72]). With  $U = 6$  m/s and  $H = 600$  m, the spring-time  $N$  value (from Figure 8b,d) is  $\sim 0.1$ , so the trade winds subsume standing rotors that recirculate air pollutants. Later in the year, rotors cause rainfall that cleans the air.

#### 4. Concluding Discussion

Meteorological influences on Caribbean air chemistry have been analyzed using in-situ, satellite and model data, with a focus on Puerto Rico. The air quality fluctuates at certain rhythms from 7-year to 10-day. Rainy weather and cleaner air prevails from June to November, so the focus was on the dry winter–spring season. Mineral dust and agricultural smoke from Africa (and South America) take many days of transport to reach the Caribbean. Along the way, the air undergoes deposition and mixing with air masses containing local urban, industrial and volcanic emissions, and pollen, bacteria, fungal spores and virus microbes. While the Saharan dust plumes are prevalent in mid-summer, hospital respiratory admissions tend to peak in March–April (cf. Figure 2f), following the sum of aerosol and trace gases: AOD f/c, AOT, BC, CO, NO<sub>2</sub>, O<sub>3</sub>, SO<sub>2</sub>. This season coincides with lowest soil moisture, increased fire emissions and high pollen loading.

Although African dust plumes join locally generated pollutants, concentrations are relatively low in the eastern Caribbean due to geographic remoteness and prevailing oceanic trade winds. Yet agricultural-industrial-urban emissions over Hispaniola, Jamaica, Puerto Rico and the southern Caribbean coast, and volcanic emissions from Montserrat contribute a noticeable burden. The statistical analysis focused on conditions over Puerto Rico in the dry season (December–May), comparing an air index with weather variables that describe local dispersion conditions. Correlations indicate that high SHF and deep PBL help to accumulate aerosols and trace gases. One of the underlying processes is the spring-season seabreeze, wherein the trade winds turn inward toward the Antilles Islands, creating hot spots. The spatial distribution of air constituents was well defined by satellite mean maps (Figure 2) while their temporal fluctuation were related to climate and weather patterns (Figures 6 and 7), thus achieving the main scientific objectives.

The spatial correlation of the daily Puerto Rico air index onto regional Tdew, air pressure and OLR December–May 2005–2015 revealed the northward movement of a dry line and trough. Hemispheric patterns show an upper trough and sub-tropical jet extending from the Caribbean toward Africa. At the climate timescale, Pacific El Niño conditions favor an increase of spring-time air pollution corresponding to anomalous inflow from Africa and the southern Caribbean coast. While the correlations inform on anomalous dispersion conditions, composites and case studies illustrate reality. Composite weather patterns for a group of high index values reflect divergent trade winds and a strong jet stream that imparts anticyclonic vorticity, subsidence and low humidity. The best-fit regression used +SHF and –Tdew to predict 22% of daily pollution variability, while soil moisture covered 82% of the mean annual cycle. This information achieves a scientific objective to underpin air quality forecasts. Regardless of time scale, surface dryness is a key indicator of terrestrial/agricultural emissions and dispersion conditions. This new understanding can underpin air quality forecasts for Puerto Rico and the wider Caribbean.

During this research, a few unexpected features emerged. The MERRA2 air index altered to bi-modal after the year 2000 with changes in GEOS5 data assimilation. Hence, climate timescale results will need updating. A counter-intuitive result was that deep PBL and higher SHF favors increased air pollution. Another strange result was the ability of OMI NO<sub>2</sub> to capture urban-industrial emissions (cf. Figure 3d) but show little sensitivity to local weather conditions (cf. Table 3). Another curious outcome was annual cycle dominance by spring-time smoke plumes (cf. Figure 3a) over summer-time aerosols and trace gases. As advocated in [73], aggregate (not individual) pollutants contribute to harmful respiratory impacts.

**Acknowledgments:** SAPSE funding support from the SA Department of Education via the University of Zululand is acknowledged. K. Matos and H. Jimenez of UPRM assisted the research. Much of the data were drawn from websites: AERONET, NASA-Giovanni, KNMI Climate Explorer, IRI Climate Library, NOAA Ready-ARL, University Wyoming Radiosonde, and LIVAS.

**Conflicts of Interest:** The authors declare no conflict of interest.

## References

1. Lim, S.S.; Vos, T.; Flaxman, A.D.; Danaei, G.; Shibuya, K.; Adair-Rohani, H.; AlMazroa, M.A.; Amann, M.; Anderson, H.R.; Andrews, K.G.; et al. A comparative risk assessment of burden of disease and injury attributable to 67 risk factors and risk factor clusters in 21 regions, 1990–2010: A systematic analysis for the Global Burden of Disease Study 2010. *Lancet* **2012**, *380*, 2224–2260. [[CrossRef](#)]
2. World Health Organization. *Air Quality Guidelines Global Update*; Report on a Working Group Meeting; World Health Organization: Geneva, Switzerland, 2005; p. 24.
3. Galanter, M.; Levy, H., II; Carmichael, G. Impacts of biomass burning on tropospheric CO, NO<sub>x</sub>, and O<sub>3</sub>. *J. Geophys. Res.* **2000**, *105*, 6633–6653. [[CrossRef](#)]
4. Longo, K.M.; Freitas, S.; Andreae, M.; Yokelson, R.; Artaxo, P. Biomass burning in Amazonia: Emissions, long-range transport of smoke and its regional and remote impacts. In *Amazonia and Global Change*; Keller, M., Bustamante, M., Gash, J., Dias, P.S., Eds.; American Geophysical Union: Washington, DC, USA, 2009; pp. 207–232.
5. Saide, P.; Bocquet, M.; Osses, A.; Gallardo, L. Constraining surface emissions of air pollutants using inverse modelling: Method intercomparison and a new two-step two-scale regularization approach. *Tellus* **2011**, *63B*, 360–370. [[CrossRef](#)]
6. Zhu, T.; Melamed, M.L.; Parrish, D.; Gauss, M.; Gallardo, L.; Lawrence, M.; Konare, A.; Liousee, C. *WMO/IGAC Impacts of Megacities on Air Pollution and Climate*; GAW Rep. 205; World Meteorological Organization: Geneva, Switzerland, 2012; p. 299.
7. Prospero, J.M.; Collard, F.X.; Molinié, J.; Jeannot, A. Characterizing the annual cycle of African dust transport to the Caribbean basin and South America and its impact on the environment and air quality. *Glob. Biogeochem. Cycles* **2014**, *28*, 757–773. [[CrossRef](#)]
8. Toro, M.V.; Cremades, L.V.; Calbó, J. Relationship between VOC and NO<sub>x</sub> emissions and chemical production of tropospheric ozone in the Aburrá Valley (Colombia). *Chemosphere* **2006**, *65*, 881–888. [[CrossRef](#)] [[PubMed](#)]
9. Bell, M.L.; Cifuentes, L.A.; Davis, D.L.; Cushing, E.; Telles, A.G.; Gouveia, N. Environmental health indicators and a case study of air pollution in Latin American cities. *Environ. Res.* **2011**, *111*, 57–66. [[CrossRef](#)] [[PubMed](#)]
10. Gallardo, L.; Escribano, J.; Dawidowski, L.; Andrade, M.F.; Osses, M. Evaluation of vehicle emission inventories for carbon monoxide and nitrogen oxides for Bogotá, Buenos Aires, Santiago, and São Paulo. *Atmos. Environ.* **2012**, *47*, 12–19. [[CrossRef](#)]
11. Romero-Lankao, P.; Qin, H.; Borbor-Cordova, M. Exploration of health risks related to air pollution and temperature in three Latin American cities. *Soc. Sci. Med.* **2013**, *83*, 110–118. [[CrossRef](#)] [[PubMed](#)]
12. Molina, L.T.; Madronich, S.; Gaffney, J.S.; Apel, E.; de Foy, B.; Fast, J.; Ferrare, R.; Herndon, S.; Jimenez, J.L.; Lamb, B.; et al. An overview of the MILAGRO 2006 campaign: Mexico City emissions and their transport and transformation. *Atmos. Chem. Phys.* **2010**, *10*, 8697–8760. [[CrossRef](#)]
13. D’Angiola, A.; Dawidowski, L.E.; Gómez, D.R.; Osses, M. On-road traffic emissions in a megacity. *Atmos. Environ.* **2010**, *44*, 483–493. [[CrossRef](#)]
14. Freitas, S.R.; Longo, K.M.; Alonso, M.F.; Pirre, M.; Marecal, V.; Grell, G.; Stockler, R.; Mello, R.F.; Gácita, M.S. PREP-CHEM-SRC-1.0: A pre-processor of trace gas and aerosol emission fields for regional and global atmospheric chemistry models. *Geosci. Model Dev.* **2011**, *4*, 419–433. [[CrossRef](#)]
15. Saide, P.; Carmichael, G.R.; Spak, S.N.; Gallardo, L.; Osses, A.E.; Mena-Carrasco, M.A.; Pagowski, M. Forecasting urban PM<sub>10</sub> and PM<sub>2.5</sub> pollution episodes in very stable nocturnal conditions and complex terrain using WRF-Chem CO tracer model. *Atmos. Environ.* **2013**, *45*, 2769–2780. [[CrossRef](#)]
16. Vargas, F.A.; Rojas, N.Y.; Pachón, J.E.; Russell, A. PM<sub>10</sub> characterization and source apportionment at two residential areas in Bogotá. *Atmos. Pollut. Res.* **2012**, *3*, 72–80. [[CrossRef](#)]
17. Burrows, J.P.; Platt, U.; Borrell, P. (Eds.) *The Remote Sensing of Tropospheric Composition from Space*; Springer: Berlin, Germany, 2011; p. 536.

18. Krotkov, N.A.; McLinden, C.A.; Li, C.; Lamsal, L.N.; Celarier, E.A.; Marchenko, S.V.; Swartz, W.H.; Bucsela, E.J.; Joiner, J.; Duncan, B.N.; et al. Aura OMI observations of regional SO<sub>2</sub> and NO<sub>2</sub> pollution changes from 2005 to 2015. *Atmos. Chem. Phys.* **2016**, *16*, 4605–4629. [[CrossRef](#)]
19. Winker, D.M.; Hunt, W.M.; McGill, M.J. Initial performance assessment of CALIOP. *Geophys. Res. Lett.* **2007**, *34*. [[CrossRef](#)]
20. Molod, A.; Takacs, L.; Suarez, M.; Bacmeister, J. Development of the GEOS-5 atmospheric general circulation model: Evolution from MERRA to MERRA2. *Geosci. Model Dev.* **2015**, *8*, 1339–1356. [[CrossRef](#)]
21. GEOS-5. Data Assimilation System. 2016. Available online: [https://gmao.gsfc.nasa.gov/pubs/docs/GEOS-5.0.1\\_Documentation\\_r3.pdf](https://gmao.gsfc.nasa.gov/pubs/docs/GEOS-5.0.1_Documentation_r3.pdf) (accessed on 4 March 2017).
22. Pearce, J.L.; Beringer, J.; Nicholls, N.; Hyndman, R.J.; Tapper, N.J. Quantifying the influence of local meteorology on air quality using generalized additive models. *Atmos. Environ.* **2011**, *45*, 1328–1336. [[CrossRef](#)]
23. Schäfer, K.; Elsasser, M.; Arteaga-Salas, J.M.; Gu, J.; Pitz, M.; Schnelle-Kreis, J.; Cyrus, J.; Emeis, S.; Prévôt, A.S.H.; Zimmermann, R. Impact of meteorological conditions on airborne fine particle composition and secondary pollutant characteristics in urban area during winter-time. *Meteorol. Z.* **2016**, *25*, 267–279. [[CrossRef](#)]
24. Goudie, A.; Middleton, N. Saharan dust storms: Nature and consequences. *Earth Sci. Rev.* **2001**, *56*, 179–204. [[CrossRef](#)]
25. Prospero, J.M.; Blades, E.; Naidu, R.; Mathison, G.; Thani, H.; Lavoie, M.C. Relationship between African dust carried in the Atlantic trade winds and surges in pediatric asthma attendances in the Caribbean. *Int. J. Biometeor.* **2008**, *52*. [[CrossRef](#)] [[PubMed](#)]
26. Estevan, R.; Antuña, J.C.; Barja, B.; Cachorro, V.E.; de Frutos, Á.M.; Berjón, A.; Toledano, C.; Torres, B.; Rodrigo, R.; Hernández, T.A.; et al. Preliminary results of aerosols measurements with sun photometer at Camagüey, Cuba. *Opt. Pura Appl.* **2011**, *44*, 99–106.
27. Nowottnick, E.; Colarco, P.R.; da Silva, A.M.; Hlavka, D.L.; McGill, M.J. The fate of Saharan dust across the Atlantic and implications for a Central American dust barrier. *Atmos. Chem. Phys.* **2011**, *11*, 8415–8431. [[CrossRef](#)]
28. Prospero, J.M.; Mayol-Bracero, O.L. Understanding the transport and impact of African dust. *Bull. Am. Meteorol. Soc.* **2013**, *94*, 1329–1337. [[CrossRef](#)]
29. Grutter, M.; Arellano, J.; Bezanilla, A.; Friedrich, M.; Plaza, E.; Rivera, C.; Stremme, W. Characterization of air pollution in Mexico City by remote sensing. In Proceedings of the EGU General Assembly Conference, Vienna, Austria, 27 April–2 May 2014; Volume 16.
30. Lopes, F.J.S.; Moreira, G.A.; Rodrigues, P.F.; Guerrero-Rascado, J.L.; Andrade, M.F.; Landolfo, E. Lidar measurements of tropospheric aerosol and water vapor profiles during the winter season campaigns over the metropolitan area of São Paulo. In Proceedings of the SPIE (the International Society for Optics and Photonics), Amsterdam, The Netherlands, 22 September 2014.
31. Dunion, J.P.; Velden, C.S. The impact of the Saharan air layer on Atlantic tropical cyclone activity. *Bull. Am. Meteorol. Soc.* **2004**, *85*, 353–365. [[CrossRef](#)]
32. Okin, G.S.; Mahowald, N.; Chadwick, O.A.; Artaxo, P. Impact of desert dust on the biogeochemistry of phosphorus in terrestrial ecosystems. *Glob. Biogeochem. Cycles* **2004**, *18*, GB2005. [[CrossRef](#)]
33. Koren, I.; Kaufman, Y.J.; Washington, R.; Todd, C.C.; Rudich, Y.; Martins, J.V.; Rosenfeld, D. The Bodélé depression: A single spot in the Sahara that provides most of the mineral dust to the Amazon forest. *Environ. Res. Lett.* **2006**, *1*. [[CrossRef](#)]
34. Jury, M.R.; Santiago, M.J. Composite analysis of dust impacts on African easterly waves in the MODIS era. *J. Geophys. Res. Atmos.* **2010**, *115*. [[CrossRef](#)]
35. Spiegel, J.K.; Buchmann, N.; Mayol-Bracero, O.L.; Cuadra-Rodriguez, L.A.; Valle-Diaz, C.J.; Prather, K.A.; Mertes, S.; Eugster, W. Do cloud properties in a Puerto Rican tropical montane cloud forest depend on occurrence of long-range transported African dust? *Pure Appl. Geophys.* **2014**, *171*, 2443–2459. [[CrossRef](#)]
36. Raga, G.; Baumgardner, D.; Mayol-Bracero, O.L. Processing of aerosol particles by mountaintop clouds in Puerto Rico. *Aerosol Air Qual. Res.* **2016**, *16*, 674–688. [[CrossRef](#)]
37. Valle-Diaz, C.; Torres-Delgado, E.; Colón-Santos, S.M.; Lee, T.; Collett, J.L., Jr.; McDowell, W.H.; Mayol-Bracero, O.L. Impact of long-range transported African dust on cloud water chemistry at a tropical montane cloud forest in northeastern Puerto Rico. *Aerosol Air Qual. Res.* **2016**, *16*, 653–664. [[CrossRef](#)]

38. Husar, R.B. Intercontinental Transport of Dust: Historical and Recent Observational Evidence. In *Intercontinental Transport of Pollutants*; Stohl, A., Ed.; Springer: Berlin, Germany, 2004; pp. 277–294.
39. Ansmann, A.; Baars, H.; Tesche, M.; Müller, D.; Althausen, D.; Engelmann, R.; Pauliquevis, T.; Artaxo, P. Dust and smoke transport from Africa to South America: Lidar profiling over Cape Verde and the Amazon rainforest. *Geophys. Res. Lett.* **2009**, *36*. [[CrossRef](#)]
40. Ben-Ami, Y.; Koren, I.; Rudich, Y.; Artaxo, P.; Martin, S.T.; Andreae, M.O. Transport of North African dust from the Bodélé depression to the Amazon Basin: A case study. *Atmos. Chem. Phys.* **2010**, *10*, 7533–7544. [[CrossRef](#)]
41. Martin, S.T.; Andreae, M.O.; Artaxo, P.; Baumgardner, D.; Chen, Q.; Goldstein, A.H.; Guenther, A.B.; Heald, C.; Mayol-Bracero, O.; McMurry, P.H.; et al. Sources and properties of Amazonian aerosol particles. *Rev. Geophys.* **2010**, *48*, RG2002. [[CrossRef](#)]
42. Freitas, S.R.; Longo, K.M.; Dias, M.A.F.S.; Dias, P.L.S.; Chatfield, R.; Prins, E.; Artaxo, P.; Grell, G.A.; Recuero, F.S. Monitoring the transport of biomass burning emissions in South America. *Environ. Fluid Mech.* **2005**, *5*, 135–167. [[CrossRef](#)]
43. Molina, L.T.; Gallardo, L.; Andrade, M.; Baumgardner, D.; Borbor-Córdova, M.; Bórquez, R.; Casassa, G.; Cereceda-Balic, F.; Dawidowski, L.; Garreaud, R.; et al. Pollution and its impact on the South American cryosphere. *Earth Future* **2015**, *3*, 345–369. [[CrossRef](#)]
44. Hamburger, T.; Matisāns, M.; Tunved, P.; Ström, J.; Calderon, S.; Hoffmann, P.; Hochschild, G.; Gross, J.; Schmeissner, T.; Wiedensohler, A.; et al. Long-term in situ observations of biomass burning aerosol at a high altitude station in Venezuela—Sources, impacts and interannual variability. *Atmos. Chem. Phys.* **2013**, *13*, 9837–9853. [[CrossRef](#)]
45. SALUD. Puerto Rico Dept of Health. 2016. Available online: <https://data.pr.gov/en/category/Salud> (accessed on 1 March 2017).
46. World Bank. *The Cost of Air Pollution: Strengthening the Economic Case for Action*; World Bank Group: Washington, DC, USA, 2016; p. 122.
47. World Health Organization. WHO Global Urban Ambient Air Pollution Database. 2016. Available online: [https://www.who.int/phe/health\\_topics/outdoorair/databases/cities/en/](https://www.who.int/phe/health_topics/outdoorair/databases/cities/en/) (accessed on 8 March 2017).
48. FAOSTAT. Food and Agriculture Organization, Statistical Database. 2016. Available online: <https://www.fao.org/faostat/> (accessed on 11 March 2017).
49. GFED. Global Fire Emission Database. 2016. Available online: <https://www.globalfiredata.org/index.html> (accessed on 28 February 2017).
50. AERONET. Aerosol Robotic Network. 2016. Available online: <https://aeronet.gsfc.nasa.gov/> (accessed on 14 March 2017).
51. Torres, O.; Bhartia, P.K.; Herman, J.R.; Sinyuk, A.; Ginoux, P.; Holben, B. A long-term record of aerosol optical depth from TOMS observations and comparison to AERONET measurements. *J. Atmos. Sci.* **2002**, *59*, 398–413. [[CrossRef](#)]
52. Torres, O.; Tanskanen, A.; Veihelmann, B.; Ahn, C.; Braak, R.; Bhartia, P.K.; Veefkind, P.; Levelt, P. Aerosols and surface UV products from Ozone Monitoring Instrument observations: An overview. *J. Geophys. Res. Atmos.* **2007**, *112*. [[CrossRef](#)]
53. Schepanski, K.; Tegen, I.; Macke, A. Comparison of satellite based observations of Saharan dust source areas. *Remote Sens. Environ.* **2012**, *123*, 90–97. [[CrossRef](#)]
54. Denjean, C.; Cassola, F.; Mazzino, A.; Triquet, S.; Chevaillier, S.; Grand, N.; Bourriane, T.; Momboisse, G.; Sellegri, K.; Schwarzenbock, A.; et al. Size distribution and optical properties of African mineral dust after 475 intercontinental transport. *J. Geophys. Res. Atmos.* **2016**, *121*, 7117–7138. [[CrossRef](#)]
55. Levy, R.C.; Mattoo, S.; Munchak, L.A.; Remer, A.L.; Sayer, A.M.; Patadia, F.; Hsu, N.C. The collection 6 MODIS aerosol products over land and ocean. *Atmos. Meas. Tech.* **2013**, *6*, 2989–3034. [[CrossRef](#)]
56. Bucsela, E.J.; Krotkov, N.A.; Celarier, E.A.; Lamsal, L.N.; Swartz, W.H.; Bhartia, P.K.; Boersma, K.F.; Veefkind, J.P.; Gleason, J.F.; Pickering, K.E. A new stratospheric and tropospheric NO<sub>2</sub> retrieval algorithm for nadir-viewing satellite instruments, applications to OMI, *Atmos. Meas. Tech.* **2013**, *6*, 2607–2626. [[CrossRef](#)]
57. Krotkov, N.; Carn, S.; Krueger, A.; Bhartia, P.; Yang, K. Band residual difference algorithm for retrieval of SO<sub>2</sub> from the Aura Ozone Monitoring Instrument (OMI). *IEEE Trans. Geosci. Remote Sens.* **2006**, *44*, 1259–1266. [[CrossRef](#)]
58. Lee, H.T.; Gruber, A.; Ellingson, R.G.; Laszlo, I. Development of the HIRS outgoing longwave radiation climate dataset. *J. Atmos. Ocean. Technol.* **2007**, *24*, 2029–2047. [[CrossRef](#)]

59. Joyce, R.J.; Janowiak, J.E.; Arkin, P.A.; Xie, P.P. CMORPH: A method that produces global precipitation estimates from passive microwave and infrared data at high spatial and temporal resolution. *J. Hydrometeorol.* **2004**, *5*, 487–503. [CrossRef]
60. LIVAS. Lidar Climatology of Vertical Aerosol Structure. 2016. Available online: <https://lidar.space.noaa.gov:8080/livas> (accessed on 18 March 2017).
61. Tapley, B.D.; Bettadpur, S.; Ries, J.C.; Thompson, P.F.; Watkins, M.M. GRACE measurements of mass variability in the earth system. *Science* **2004**, *305*. [CrossRef] [PubMed]
62. Kanamitsu, M.; Ebisuzaki, W.; Woollen, J.; Yang, S.; Hnilo, J.J.; Fiorino, M.; Potter, G.L. NCEP–DOE AMIP-II Reanalysis-2. *Bull. Am. Meteorol. Soc.* **2002**, *83*, 1631–1643. [CrossRef]
63. LARC. NASA Website for CALIPSO Data. 2016. Available online: <https://www-calipso.larc.nasa.gov> (accessed on 18 March 2017).
64. Stein, A.F.; Draxler, R.R.; Rolph, G.D.; Stunder, B.J.; Cohen, M.D.; Ngan, F. NOAA’s HYSPLIT atmospheric transport and dispersion modeling system. *Bull. Am. Meteorol. Soc.* **2015**, *96*, 2059–2077. [CrossRef]
65. Chen, Z.; Cai, J.; Gao, B.; Xu, B.; Dai, S.; He, B.; Xie, X. Detecting the causality influence of individual meteorological factors on local PM<sub>2.5</sub> concentration in (China’s) Jing-Jin-Ji region. *Nat. Sci. Rep.* **2017**, *7*. [CrossRef]
66. Ostro, B.; Lipsett, M.; Mann, J.; Braxton-Owens, H.; White, M. Air pollution and exacerbation of asthma in African-American children in Los Angeles. *Epidemiology* **2001**, *12*, 200–208. [CrossRef] [PubMed]
67. Kanyanga, J.K. El Nino Southern Oscillation (ENSO) and Atmospheric (Aerosol) Transport over Southern Africa. Ph.D. Thesis, University of the Witswatersrand, Johannesburg, South Africa, 2008.
68. Newhouse, C.P.; Levetin, E. Correlation of environmental factors with asthma and rhinitis symptoms in Tulsa, OK. *Ann. Allergy Asthma Immunol.* **2004**, *92*, 356–366. [CrossRef]
69. Gent, J.F.; Triche, E.W.; Holford, T.R.; Belanger, K.; Bracken, M.B.; Beckett, W.S.; Leaderer, B.P. Association of low-level ozone and fine particles with respiratory symptoms in children with asthma. *J. Am. Med. Assoc.* **2003**, *290*, 1859–1867. [CrossRef] [PubMed]
70. Pielke, R.A.; Segal, M. Mesoscale circulations forced by differential terrain heating. In *Mesoscale Meteorology and Forecasting*; Ray, P.S., Ed.; American Meteorological Society: Boston, MA, USA, 1986; pp. 516–548.
71. Smolarkiewicz, P.K.; RRasmussen, M.; Clark, T.L. On the dynamics of Hawaiian cloud bands: Island forcing. *J. Atmos. Sci.* **1988**, *45*, 1872–1905. [CrossRef]
72. Smith, R.B.; Gleason, A.C.; Gluhosky, P.A.; Grubisic, V. The wake of St. Vincent. *J. Atmos. Sci.* **1997**, *54*, 606–623. [CrossRef]
73. Ortiz-Martínez, M.; Rodríguez-Cotto, R.I.; Ortiz-Rivera, M.A.; Pluguez-Turull, C.W.; Jiménez-Vélez, B.D. Linking endotoxins, African dust PM<sub>10</sub> and asthma in an urban and rural environment of Puerto Rico. *Med. Inflamm.* **2015**. [CrossRef] [PubMed]

